# X-ray Diffraction and Computation Yield the Structure of Alkanethiols on Gold(111)

A. Cossaro, *et al.*

*Science* **321**, 943 (2008);
DOI: 10.1126/science.1158532



*Science* (print ISSN 0036-8075; online ISSN 1095-9203) is published weekly, except the last week in December, by the American Association for the Advancement of Science, 1200 New York Avenue NW, Washington, DC 20005. 

surface, may produce arrays with better placement accuracy than the accuracy demonstrated here, as well as higher aspect ratio features. Well-ordered block copolymer arrays may be useful as etch masks in a range of applications, such as patterned recording media, that require periodic nanoscale features covering large areas. This templating approach thus provides a method of combining top-down and bottom-up nanopatterning techniques, where information is placed on the substrate by writing a sparse lattice of posts, and the self-assembling material spontaneously populates the empty spaces on the template with a seamless nanostructured array of determined orientation and lattice spacing.


**References and Notes**

1. C. D. Bain *et al.*, *J. Am. Chem. Soc.* **111**, 321 (1989).
2. B. O. Dabbousi, C. B. Murray, M. F. Rubner, M. G. Bawendi, *Chem. Mater.* **6**, 216 (1994).
3. Y. Yin, Y. Xia, *Adv. Mater.* **13**, 267 (2001).
4. M. J. Fasolka, A. M. Mayes, *Annu. Rev. Mater. Res.* **31**, 323 (2001).
5. P. Mansky, P. Chaikin, E. L. Thomas, *J. Mater. Sci.* **30**, 1987 (1995).
6. M. Park, C. Harrison, P. M. Chaikin, R. A. Register, D. H. Adamson, *Science* **276**, 1401 (1997).
7. R. G. H. Lammertink *et al.*, *Adv. Mater.* **12**, 98 (2000).
8. T. Thurn-Albrecht *et al.*, *Science* **290**, 2126 (2000).
9. J. Y. Cheng *et al.*, *Adv. Mater.* **13**, 1174 (2001).
10. Y. S. Jung, C. A. Ross, *Nano Lett.* **7**, 2046 (2007).
11. C. Park, J. Yoon, E. L. Thomas, *Polymer* **44**, 6725 (2003).
12. R. A. Segalman, *Mater. Sci. Eng. Rep.* **48**, 191 (2005).
13. S. B. Darling, *Prog. Polym. Sci.* **32**, 1152 (2007).
14. R. A. Segalman, H. Yokoyama, E. J. Kramer, *Adv. Mater.* **13**, 1152 (2001).
15. J. Y. Cheng, C. A. Ross, E. L. Thomas, H. I. Smith, G. J. Vancso, *Appl. Phys. Lett.* **81**, 3657 (2002).
16. J. Y. Cheng, A. M. Mayes, C. A. Ross, *Nat. Mater.* **3**, 823 (2004).
17. L. Rockford *et al.*, *Phys. Rev. Lett.* **82**, 2602 (1999).
18. S. O. Kim *et al.*, *Nature* **424**, 411 (2003).
19. E. W. Edwards, M. F. Montague, H. H. Solak, C. J. Hawker, P. F. Nealey, *Adv. Mater.* **16**, 1315 (2004).
20. M. P. Stoykovich *et al.*, *Science* **308**, 1442 (2005).
21. J. Y. Cheng, C. T. Rettner, D. P. Sanders, H. C. Kim, W. D. Hinsberg, *Adv. Mater.*, published online 7 July 2008; 10.1002/adma.200800826.
22. R. Ruiz *et al.*, *Science* **321**, 936 (2008).
23. J. K. W. Yang, K. K. Berggren, *J. Vac. Sci. Technol. B* **25**, 2025 (2007).
24. G. J. Kellogg *et al.*, *Phys. Rev. Lett.* **76**, 2503 (1996).
25. D. J. Kinning, E. L. Thomas, *Macromolecules* **17**, 1712 (1984).
26. E. Helfand, *Acc. Chem. Res.* **8**, 295 (1975).
27. P. G. de Gennes, *Macromolecules* **13**, 1069 (1980).



28. The financial support of the National Science Foundation, the Semiconductor Research Corporation, the Nanoelectronics Research Initiative, King Abdullaziz City for Science and Technology and Alfaisal University, and the Singapore-MIT Alliance is appreciated. The Research Laboratory of Electronics Scanning-Electron-Beam Lithography Facility was used for this work. We thank M. Mondol and J. Daley for technical assistance. The authors declare no competing interests.


**Supporting Online Material**

www.sciencemag.org/cgi/content/full/321/5891/939/DC1
Materials and Methods
SOM Text
Figs. S1 and S2
Tables S1 and S2
References


21 April 2008; accepted 11 July 2008
10.1126/science.1159352


# X-ray Diffraction and Computation Yield the Structure of Alkanethiols on Gold(111)


A. Cossaro,[1] R. Mazzarello,[2] R. Rousseau,[2]* L. Casalis,[3] A. Verdini,[1] A. Kohlmeyer,[4] L. Floreano,[1] S. Scandolo,[5] A. Morgante,[1,6]† M. L. Klein,[4] G. Scoles[2,3,7]



The structure of self-assembled monolayers (SAMs) of long-chain alkyl sulfides on gold(111) has been resolved by density functional theory–based molecular dynamics simulations and grazing incidence x-ray diffraction for hexanethiol and methylthiol. The analysis of molecular dynamics trajectories and the relative energies of possible SAM structures suggest a competition between SAM ordering, driven by the lateral van der Waals interaction between alkyl chains, and disordering of interfacial Au atoms, driven by the sulfur-gold interaction. We found that the sulfur atoms of the molecules bind at two distinct surface sites, and that the first gold surface layer contains gold atom vacancies (which are partially redistributed over different sites) as well as gold adatoms that are laterally bound to two sulfur atoms.


Self-assembled monolayers (SAMs) of alkyl sulfides on metal surfaces have many potential applications in molecular electronics, biosensors, and nanopatterning (*1*–*3*). In the high-coverage regime, the molecules are anchored to the metal substrate through their sulfur termination S, and the alkyl chains R [where R = $(CH_2)_nCH_3$] point away from the surface. Gold is the most commonly used substrate in sulfur-containing SAMs, in part because of the strong Au-S interaction.

However, despite many years of research on these systems, the nature of the Au-S interaction is still debated. Only recently has the role of the underlying Au substrate in the chemisorption of thiols been recognized, for both crystal and nanoparticle (NP) surfaces (*4*–*7*). For the short-chain limit (R = $CH_3$), the presence of adatoms and vacancies plays a crucial role in this process. Surface complexes wherein two S atoms are joined by an intermediate Au adatom (RS-Au-SR) have been observed experimentally at both low (*4*) and high coverage (*5*); this finding has been supported, and in certain cases predicted, by density functional theory (DFT) (*5*, *8*, *9*). Similar Au-SR motifs were recently identified at the surface of thiol-protected Au NPs (*10*).

It is natural to assume that these species are also present at the Au-SR interface of the long-chain SAMs (*11*). We now show that the energetics of the gold-SAM interface, in competition with the molecular packing forces arising from the alkyl chains at high coverage, lead to the formation of a commensurate superstructure, conventionally known as *c*(4×2) (*12*), in which the hydrocarbon chains tilt by about 30° from the surface normal. This structure yields the close packing that provides these SAMs with their technologically useful "passivating" properties (*2*, *13*–*15*).

Most of the structural models proposed so far for the *c*(4×2) superstructure have assumed that the Au(111) substrate remains flat and defect-free; they explain the superstructure in terms of nonequivalent chain torsion angles (*16*), sulfur dimerization (*15*), or differences in adsorption sites (*7*, *17*) [for a review, see (*18*)]. Only a few experimental investigations have been interpreted in terms of a more complex landscape at the interface. The alternatives included an Au atom rippling (*19*) and an increase in either the substrate roughness (*20*) or the density of defects (*21*). A recent theoretical study of intermediate-length alkyl sulfides on Au(111), which started from the results obtained in our previous work for $CH_3S$ [methylthiol (MT)] SAMs (*5*), found that the RS-Au-SR motif is also energetically competitive for SAMs of the $SC_nH_m$ moiety on Au(111) surfaces and is consistent with SAM corrugations seen in scanning tunneling microscopy (STM) images (*22*).

Here, we show that the existence of the RS-Au-SR structural motif for the case of longer alkanethiols is confirmed by a DFT-based theoretical simulation of the system that includes the lateral van der Waals interactions between the alkyl chains, as well as by a thorough analysis of extensive grazing incidence x-ray diffraction (GIXRD) experiments. Furthermore, DFT-based molecular dynamics (MD) simulations reveal the


[1]Istituto Nazionale per la Fisica della Materia–Consiglio Nazionale delle Ricerche (INFM-CNR) Laboratorio TASC, I-34012 Trieste, Italy. [2]International School for Advanced Studies, I-34014 Trieste, Italy. [3]Sincrotrone Trieste S.C.p.A., I-34012 Trieste, Italy. [4]Center for Molecular Modeling and Department of Chemistry, University of Pennsylvania, Philadelphia, PA 19104, USA. [5]Abdus Salam International Centre for Theoretical Physics and INFM/Democritos National Simulation Center, I-34014 Trieste, Italy. [6]Department of Physics, University of Trieste, I-34127 Trieste, Italy. [7]Department of Chemistry, Princeton University, Princeton, NJ 08544, USA.

*Present address: Pacific Northwest National Laboratory, Richland, WA 99352, USA.

†To whom correspondence should be addressed. E-mail: morgante@tasc.infm.it

presence at the buried interface of both Au adatoms and vacancies in the first layer, which provides, as in the case of $CH_3S$ (*5*), a structural model that fits the x-ray data with great accuracy. We chose to focus on hexanethiol (HT) [R = $(CH_2)_5CH_3$], which is known to form a $c(4\times2)$ superstructure in coexistence with only minor amounts of the $(\sqrt{3}\times\sqrt{3})$ phase (*18*), because for shorter chains the equilibrium between the two structures has not been as clearly determined.

The nature of the potential energy landscape for SR adsorption can be understood by considering the adsorption energy $E_{ad}$ for a variety of structures. In agreement with experiments (*23*), the $E_{ad}$ values of HT are similar to those already reported for methylthiol (*5*, *22*, *24*). Without gold vacancies, the preferred configuration corresponds to the RS-Au-SR motif (Fig. 1), with $E_{ad}$ = 2.0 eV ($E_{ad}$ = 1.9 eV for MT). An on-top site is 0.5 eV higher in energy for both molecules, whereas the bridge site is 0.2 eV higher for MT but only 0.1 eV higher for HT. The energetic cost for the formation of a vacancy is about 0.5 eV for the passivated Au surface, which is more than compensated by an increase in the binding of the adsorbate. Thus, the bridge site becomes energetically competitive with that of the RS-Au-SR motif when vacancies are added; for example, one vacancy per thiol yields $E_{ad}$ = 2.0 eV for HT and 1.8 eV for MT. Indeed, several models with both RS-bridge and RS-Au-SR motifs and one to three vacancies per $c(4\times2)$ cell are found to be energetically favorable ($E_{ad}$ = 1.9 to 2.0 eV) (*22*). The existence of these almost isoenergetic adsorption species suggests that the potential energy surface for thiol adsorption is extremely flat; hence, both static and dynamic disorder are expected to play a key role at the Au(111) interface. It follows that, solely on the basis of $T$ = 0 K calculations, DFT is unlikely to predict the difference of behavior between short- and long-chain thiols, nor to assign the structure to a single potential energy minimum.

To obtain a qualitative understanding of how the short- and long-chain species differ, we considered a series of DFT-based MD runs on HT and MT (*5*) SAMs. Small-cell MD simulations of four HT SAMs and two initial vacancies were performed at 300 and 500 K, starting from an on-top structure. The formation of an adatom added another vacancy, corresponding to a total 0.25 of an Au monolayer (ML). In these simulations, the alkyl chains hampered the dynamics; as a consequence, the amount of interconversion (Fig. 1E) between different structures was strongly reduced with respect to MT. The on-top site readily collapsed to a lower-energy structure for both MT and HT, but this process required 4 ps for HT at 500 K, versus <1 ps for MT at similar temperatures. At 300 K, the formation of RS-Au-SR species occurred for MT after 4 ps but was not observed with HT for the 10-ps duration of the simulation.

We also conducted 16-molecule simulations at 300 K starting from a repeated $(2\sqrt{3}\times3)$ superstructure consisting of eight bridges, four HT-Au-HT species, and eight vacancies. Here, bridge and HT-Au-HT configurations remained in equilibrium for the duration of the simulation. The slowing of dynamical processes can be seen in the probability plots of position distribution relative to an underlying $(\sqrt{3}\times\sqrt{3})$ cell in Fig. 1, A to D. Unimodal Au and S position distributions are found for HT, whereas those of MT are broader and often bimodal. All of the simulations show that HT chains retained a well-ordered hexagonal array with a tilt angle of about 30° with respect to the surface normal (Fig. 1F). This result is at variance with the MT case, where the surface was more dynamic and methyl groups did not show any short-range order.

Our DFT data suggest that several key aspects are needed to fit the $c(4\times2)$ structure: (i) Adatoms and vacancies should be present at the surface in similar concentrations, as found for MT (*5*), but more localized because of the hindered S-Au motion imposed by the longer alkyl chains; (ii) sulfur atoms should be located in either the bridge or RS-Au-SR configurations in roughly equal proportions; and (iii) the alkyl chains should retain a well-ordered hexagonal array with a height corrugation of about 0.6 Å.

The presence of vacancy and adatom defects on the gold surface is strongly supported by the GIXRD data. The similarities of some scans [(0, 0) and (4, –2); Fig. 2] with the equivalent ones taken on the $(\sqrt{3}\times\sqrt{3})$ MT phase (*5*) indicate that the two systems have common morphological and structural features. In particular, the drop in the x-ray reflectivity [the (0, 0) rod] of the two systems is similar and suggests analogous vacancy and adatom distribution probabilities (atomic roughness) at the molecule-gold interface.

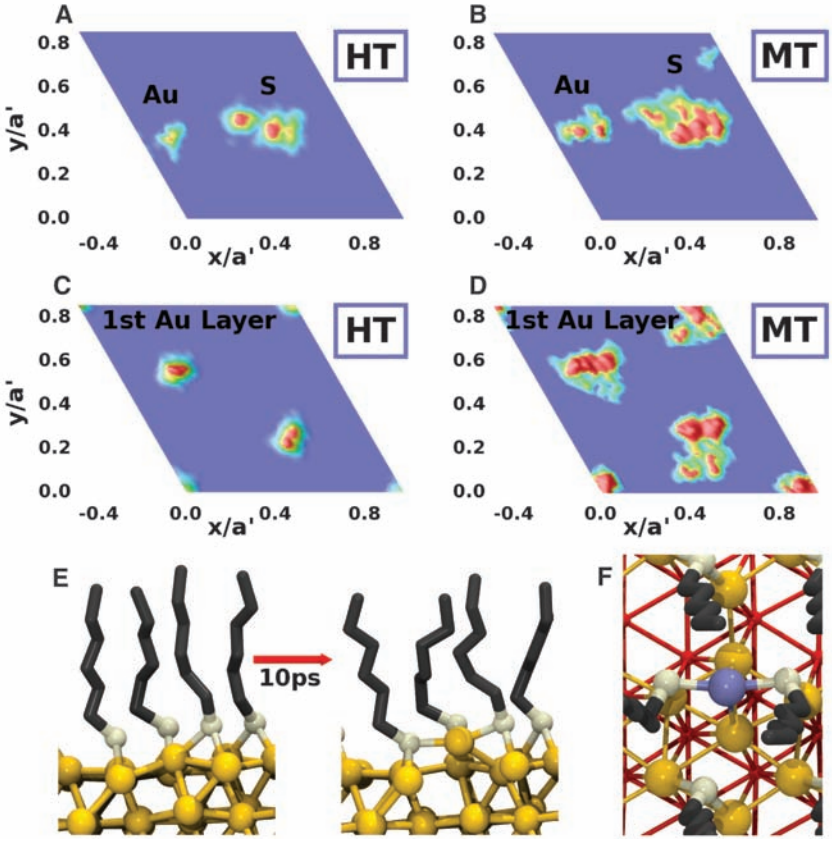


**Fig. 1.** Top view of the Au(111) surface and selected MD results. (**A** to **D**) Position density distributions, $P(x,y)$, for HT (16-molecule cell) and MT [from (*5*)] projected into the $(\sqrt{3}\times\sqrt{3})$ cell ($a'$ = 4.99 Å). (A) Au adatom and S for HT, (B) Au adatom and S for MT; S shows two unimodal positions in (A) due to poor interconversion between bridge and RS-Au-SR configurations, whereas for MT (B) all positions are multimodal because of interconversion. (C) First Au layer for HT, (D) first Au layer for MT; all positions are unimodal and near the ideal lattice site for HT, but bimodal with large deviations from ideal lattice for MT. (**E**) MD snapshots separated by 10 ps at 500 K from 4-HT cell, showing formation of HT-Au-HT species (light yellow, S; black, C; dark yellow, Au); H atoms are not shown. (**F**) Average structure positions from 16-HT cell; colors are as in (E), except adatom labeled in blue and second Au layer marked in red. HT SAM exhibits hexagonal packing of the chains that are tilted off the normal by 30°, irrespective of the binding site. Au-S bond lengths are 2.45 Å for the bridge configuration, whereas lengths of 2.33 Å are found between the S and adatom in RS-Au-SR (compare with Table 1); S atoms display different heights of 2.0 Å and 2.6 Å above the surface for bridge and S-Au-S structures, respectively. This height corrugation is preserved in the height of chains.

The interface model found for the MT surface (*5*) was used as a starting point for the GIXRD analysis. As in that case, partially occupied atomic sites were adopted in the first Au layer to simulate the dynamical disorder induced by the interconversion between the two different thiol adsorption geometries plus vacancy migration. In agreement with our calculations, the fits yielded a model wherein adatoms and vacancies were delocalized over fewer sites than in the MT case. Best-fit conditions were found for a model where the topmost Au layer contained 2.8 vacancies per $(2\sqrt{3} \times 3)$ unit cell (0.7 vacancies per HT), equivalent to 0.23 ML. The vacancy population was distributed over only two pairs of equivalent sites; that is, the vacancies were less delocalized than in the MT system, where we found 0.6 vacancies per $(\sqrt{3} \times \sqrt{3})$ unit cell (0.6 vacancies per MT), equivalent to 0.2 ML.

The adatom was delocalized over only two symmetry-equivalent atomic sites (half a site per HT, versus one site per thiol in the case of MT), with the same 0.6 occupancy (0.3 adatoms per HT, i.e., adatom coverage of 0.1 ML), and was located in such a way that the average structure consisted of -S-Au-S-Au-S- one-dimensional zigzag chains aligned along the cell short axis (Fig. 3). Zigzag chains of this type are frequently observed in STM experiments on SAMs (*18*, *25*, *26*). With the caveat that the occupation of the adatom sites is here only partial because of dynamical fluctuations, such chains are nonetheless reminiscent of the "polymeric" zigzag motifs proposed for MT-Au(111) (*9*) and for MT on Au NPs (*6*). For the sake of clarity, only the topmost Au layer, the Au adatoms, and the S atoms are shown in Fig. 3. The second Au layer presents minor lateral ditortions, whereas the structure of the third and fourth layers is only slightly affected by the reconstruction.

The relative positions between Au adatoms and S atoms (i.e., molecules) derived by the GIXRD analysis are consistent with our theoretical model, wherein two molecules on the on-top site form the RS-Au-SR motif and the other two molecules adsorb on bridge sites. The coordinates of the first-layer Au atoms and molecules are reported in Table 1 (*27*). Although the fit of GIXRD is not very sensitive to the polar orientation of the molecular chains, the best fit yields an angle of 35° ± 10° with respect to the surface normal, in fair agreement with theory.

We note that in the common range of scanned reciprocal space, our GIXRD data are in good agreement with previous studies (*15*, *17*, *19*). With respect to previous interpretations, the model proposed here reconciles theoretical calculations and interpretation of experimental results. We found that the $c(4\times2)$ superstructure of long-chain alkyl sulfides results from an approximate population of 2.8 vacancies and 1.2 adatoms per $(2\sqrt{3} \times 3)$ cell and a limited interconversion between RS-Au-SR and RS-bridge structures. Although the SAM is ordered, the Au-S interface is affected by a dynamical disorder because of the partial delocalization of vacancies and adatoms. The constraint of the ordered SAM, driven by alkyl-chain packing, leads to a partial ordering at the interface and hence a superstructure of the $(\sqrt{3} \times \sqrt{3})$ lattice.

These findings strongly underscore the importance of the underlying Au-S interactions and support some recent single-molecule conductance measurements of the Au-dithiol system that have shown junctions differing in space and time because of both static and dynamic disorder (*28*).

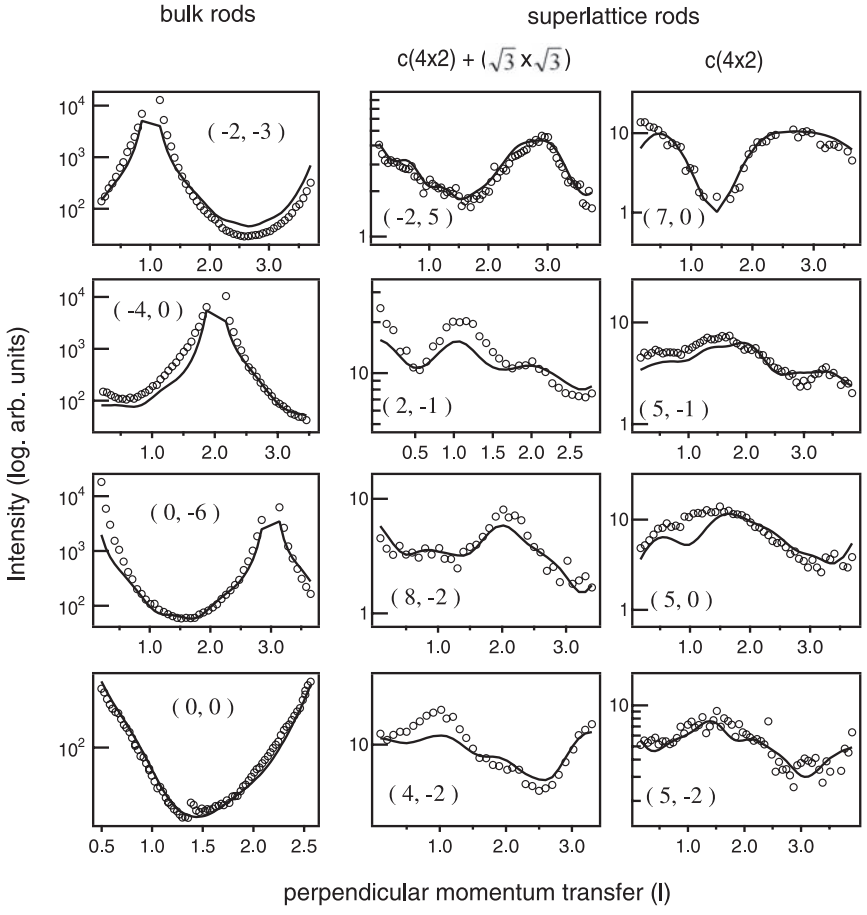


**Fig. 2.** X-ray diffraction rod data and fitting curves (solid lines) as a function of the perpendicular momentum transfer in $l$ units [$l = 2\pi/c$, where $c$ is the vector of the unit cell along the surface normal $z$ ($c$ = 7.06 Å)]. Bulk rods are reported in the left panel. Rods in the right panel refer to reciprocal lattice points that are common to both the $\sqrt{3} \times \sqrt{3}$ and $c(4\times2)$ superlattices; rods at the far right refer to the $c(4\times2)$ superlattice only. See supporting online material for further details.

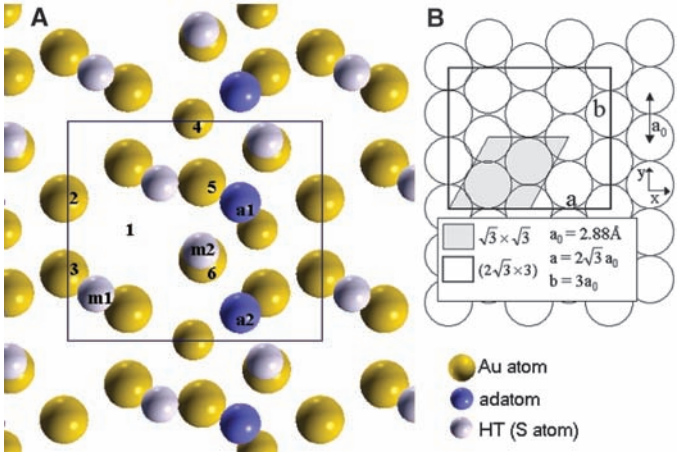


**Fig. 3.** (**A**) Top view of the model resulting from GIXRD fit. Only the topmost Au layer with adatoms and S atoms of molecules are indicated. (**B**) Top view of the Au(111) surface with indications of the unit cells mentioned in the text. The conventionally termed $c(4\times2)$ corresponds to $c(2\sqrt{3} \times 4\sqrt{3})$, whose primitive cell is $(2\sqrt{3} \times 3)$, as depicted in the model. Note that as a result of the zigzag geometrical constraint (see text for explanation), the two S atoms in bridge sites [labeled m1 in (A)] are inequivalent because they bridge two different Au pairs, namely the atom pairs 3-2 and 3-5. The average S-Au bond length results are 2.42 Å and 2.37 Å for RS in bridge and RS-Au-SR geometry, respectively.

**Table 1.** Atomic positions and occupations from GIXRD analysis. Au1 to Au6 are the Au atoms in the first Au surface layer, a1 and a2 are the Au adatoms, and m1 and m2 are the S atoms.

| | Occupancy | *x/a* | *y/b* | *z/c* |
|---|---|---|---|---|
| | (±0.05) | | (±0.008) | |
| Au1 | 0 | — | — | — |
| Au2 | 1 | −0.011 | 0.624 | −0.045 |
| Au3 | 1 | −0.010 | 0.283 | −0.025 |
| Au4 | 0.6 (±0.1) | 0.493 | 0.985 | −0.022 |
| Au5 | 1 | 0.527 | 0.697 | +0.025 |
| Au6 | 1 | 0.530 | 0.351 | +0.033 |
| a1 | 0.6 (±0.1) | 0.678 | 0.610 | 0.294 |
| a2 | 0.6 (±0.1) | | a1 − b/2 | |
| m1 | — | 0.113 | 0.193 | 0.265 |
| m2 | — | 0.523 | 0.396 | 0.365 |

As a consequence of these findings, studies regarding the formation, growth, diffusion, and mechanical properties of these films may need to be revisited in order to properly account for the influence of Au-S interactions and the presence of the RS-Au-SR structural motifs. From a theoretical perspective, this gives paramount importance to the development of empirical potential models that include not only molecule-molecule interactions but explicitly the Au-SR interactions, which are often neglected. In addition, our findings indicate that the adatom structures will alter the local density of states at the Fermi energy (*18*) and will affect the interpretation of electronic and magnetic properties of these materials.

### References and Notes


1. A. Ulman, *Chem. Rev.* **96**, 1533 (1996).
2. F. Schreiber, *Prog. Surf. Sci.* **65**, 151 (2000).
3. J. C. Love *et al.*, *Chem. Rev.* **105**, 1103 (2005).
4. P. Maksymovych *et al.*, *Phys. Rev. Lett.* **97**, 146103 (2006).
5. R. Mazzarello *et al.*, *Phys. Rev. Lett.* **98**, 016102 (2007).
6. H. Hakkinen *et al.*, *J. Phys. Chem. B* **110**, 9927 (2006).
7. M. Yu *et al.*, *Phys. Rev. Lett.* **97**, 166102 (2006).
8. A. Nagoya *et al.*, *J. Phys. Cond. Matter* **19**, 365245 (2007).
9. H. Grönbeck *et al.*, *J. Phys. Chem. B* **111**, 3325 (2007).
10. P. D. Jadzinsky *et al.*, *Science* **318**, 430 (2007).
11. R. L. Whetten, R. C. Price, *Science* **318**, 407 (2007).
12. The conventionally termed $c(4\times2)$ corresponds to a $c(2\sqrt{3}\times4\sqrt{3})$, whose primitive cell is $(2\sqrt{3}\times3)$.
13. R. G. Nuzzo *et al.*, *J. Chem. Phys.* **93**, 767 (1990).
14. N. Camillone *et al.*, *J. Chem. Phys.* **98**, 3503 (1993).
15. P. Fenter, A. Eberhardt, P. Eisenberger, *Science* **266**, 1216 (1994).
16. D. Anselmetti *et al.*, *Europhys. Lett.* **27**, 365 (1994).
17. X. Torrelles *et al.*, *J. Phys. Chem. B* **110**, 5586 (2006).
18. C. Vericat *et al.*, *J. Phys. Cond. Matter* **18**, R867 (2006).
19. X. Torrelles *et al.*, *Langmuir* **20**, 9396 (2004).
20. M. C. Gerstenberg *et al.*, *Phys. Rev. B* **61**, 7678 (2000).
21. M. Prato *et al.*, *J. Phys. Chem. C* **112**, 3899 (2008).
22. J. G. Wang *et al.*, *J. Phys. Chem. C* **111**, 12149 (2007).
23. D. J. Lavrich *et al.*, *J. Phys. Chem. B* **102**, 3456 (1998).
24. M. C. Vargas *et al.*, *J. Phys. Chem. B* **105**, 9509 (2001).
25. G. E. Poirier, *Langmuir* **15**, 1167 (1999).
26. A. Riposan *et al.*, *J. Phys. Chem. B* **110**, 23926 (2006).
27. In our structural determination, the distance of the Au adatoms from a Au(111) crystal plane is an integer multiple of the Au lattice constant, consistent with the Au coherent fraction of the x-ray standing wave measured in (*29*).
28. J. Ulrich *et al.*, *J. Phys. Chem. B* **110**, 2462 (2006).
29. P. Fenter *et al.*, *Surf. Sci.* **412–413**, 213 (1998).


30. We thank INFM's Parallel Computing Initiative and the San Diego Supercomputing Center (SDSC) for CPU time, and M. Tatineni at SDSC for help with getting early access to new TeraGrid resources. Supported by Ministero dell'Università e della Ricerca PRIN 2006020543 and FIRB NOMADE and by NSF grant CHE-0626354.


### Supporting Online Material

www.sciencemag.org/cgi/content/full/321/5891/943/DC1
Materials and Methods
References

1 April 2008; accepted 8 July 2008
10.1126/science.1158532

# Smoke Invigoration Versus Inhibition of Clouds over the Amazon

**Ilan Koren,[1] J. Vanderlei Martins,[2,3] Lorraine A. Remer,[3] Hila Afargan[1]**

**The effect of anthropogenic aerosols on clouds is one of the most important and least understood aspects of human-induced climate change. Small changes in the amount of cloud coverage can produce a climate forcing equivalent in magnitude and opposite in sign to that caused by anthropogenic greenhouse gases, and changes in cloud height can shift the effect of clouds from cooling to warming. Focusing on the Amazon, we show a smooth transition between two opposing effects of aerosols on clouds: the microphysical and the radiative. We show how a feedback between the optical properties of aerosols and the cloud fraction can modify the aerosol forcing, changing the total radiative energy and redistributing it over the atmospheric column.**

The effect of aerosols on clouds and precipitation contributes the largest uncertainty to the estimation of the anthropogenic contribution to climate change. There are two main pathways by which aerosols can change cloud properties: microphysical and radiative processes (*1*, *2*). Changes in aerosol particle concentration produce changes in the size distribution of the cloud droplets (because aerosols function as cloud condensation nuclei) and therefore affect condensation and evaporation rates, latent heat release, collision coalescence efficiency, and related cloud properties such as reflectance, lifetime, phase, size, and precipitation (*3*–*5*).

[1]Department of Environmental Sciences, Weizmann Institute, Rehovot 76100, Israel. [2]Department of Physics and Joint Center for Earth Systems Technology, University of Maryland Baltimore County, Baltimore, MD 21250, USA. [3]Laboratory for Atmospheres, NASA Goddard Space Flight Center, Greenbelt, MD 20771, USA.

Additionally, the absorption of aerosols can change the atmospheric stability profile by heating the aerosol layer and cooling the layers below. This may stabilize shallow layers and reduce their relative humidity, suppress moisture and heat fluxes from the surface, and suppress shallow cloud formation inside or below the aerosol layer (*6*, *7*), while destabilizing the profile above the aerosol layer.

The microphysical and the radiative pathways of interaction initiate many feedbacks that add complexity to the system and have different sensitivities to the aerosol loading. Clouds are sensitive to the initial concentration and size distribution of the potential cloud condensation nuclei (CCN). For a given aerosol type (size distribution and chemistry), clouds have a logarithmic sensitivity to the amount of potential CCN (*8*–*10*). Small changes in the aerosol loading in clean environments (a low CCN concentration of ~100 CCN/cm$^3$) will potentially change the cloud properties (fraction, optical depth, and droplet size distribution) much more than similar changes when the cloud is polluted (a CCN concentration of ~1000 CCN/cm$^3$) and the effect approaches saturation. In contrast, the absorption of electromagnetic energy (mostly in the visible and near-infrared range) by aerosols has a completely different sensitivity to aerosol loading. The overall absorption of energy increases steadily with the aerosol loading, and the increasing rate depends on the diurnal cycle of solar flux (geometry), aerosol optical properties, surface albedo, and the depths of the aerosol layer (*11*).

In this paper, we develop a theoretical basis that ties together the two pathways and explores the relationships of cloud amount and vertical development to aerosol optical thickness (τ), a proxy for CCN and for the potential to absorb solar energy. We find a smooth transition between these two pathways in an observational data set obtained over the Amazon.

The (aerosol) absorption (cloud) fraction feedback (AFF) can be described as follows: Aerosol absorption of solar radiation heats the aerosol layer and cools the surface, stabilizing the temperature profile and reducing relative humidity and surface moisture fluxes (evapotranspiration). This effect reduces cloudiness. Reduced cloud coverage exposes greater areas of the aerosol layer to direct fluxes from the Sun and therefore produces more intense heating of the aerosol layer, further reducing cloudiness. This positive feedback will be balanced once the extra heating of the surface raises the surface temperature sufficiently to destabilize the profile again and to transfer the humidity concentrated